

Interferometric phase reconstruction using simplified coherence network



Kui Zhang^{a,*}, Ruiqing Song^b, Hui Wang^a, Di Wu^a, Hua Wang^c

^a College of Communication Engineering, Chongqing University, Chongqing 400044, China

^b Institute of Earthquake Science, China Earthquake Administration, Beijing 100036, China

^c Department of Surveying Engineering, Guangdong University of Technology, Guangzhou 510643, China

ARTICLE INFO

Article history:

Received 29 December 2015

Received in revised form 3 May 2016

Accepted 4 May 2016

Keywords:

Persistent scatterer interferometry

Interferometric stacking techniques

Phase reconstruction

Coherence matrix

Simplified coherence network

ABSTRACT

Interferometric time-series analysis techniques, which extend the traditional differential radar interferometry, have demonstrated a strong capability for monitoring ground surface displacement. Such techniques are able to obtain the temporal evolution of ground deformation within millimeter accuracy by using a stack of synthetic aperture radar (SAR) images. In order to minimize decorrelation between stacked SAR images, the phase reconstruction technique has been developed recently. The main idea of this technique is to reform phase observations along a SAR stack by taking advantage of a maximum likelihood estimator which is defined on the coherence matrix estimated from each target. However, the phase value of a coherence matrix element might be considerably biased when its corresponding coherence is low. In this case, it will turn to an outlying sample affecting the corresponding phase reconstruction process. In order to avoid this problem, a new approach is developed in this paper. This approach considers a coherence matrix element to be an arc in a network. A so-called simplified coherence network (SCN) is constructed to decrease the negative impact of outlying samples. Moreover, a pointed iterative strategy is designed to resolve the transformed phase reconstruction problem defined on a SCN. For validation purposes, the proposed method is applied to 29 real SAR images. The results demonstrate that the proposed method has an excellent computational efficiency and could obtain more reliable phase reconstruction solutions compared to the traditional method using phase triangulation algorithm.

© 2016 International Society for Photogrammetry and Remote Sensing, Inc. (ISPRS). Published by Elsevier B.V. All rights reserved.

1. Introduction

In order to overcome the main drawbacks of the conventional differential interferometric synthetic aperture radar (DInSAR) technique (e.g. geometrical/temporal decorrelation, atmospheric phase delay), the persistent scatterer interferometry (PSI) technique (Crosetto et al., 2016) has been systematically proposed in the early 2000s (Ferretti et al., 2000, 2001). Due to its successful applications in deformation monitoring (Hooper et al., 2004; Peltier et al., 2010; Ciampalini et al., 2014; Graniczny et al., 2015; Terranova et al., 2015), it has already attracted increasing attention in the last decade. The basic idea of such techniques is to separate interferometric phase components on point-wise targets from a stack of interferograms by taking advantage of their different time-spatial behaviors. Such point-wise targets, referred to as per-

manent scatterers (PS), are highly coherent even in long geometrical and temporal baseline spans. For commonly used C-band SAR data, the spatial density of PS in urban areas can be larger than 100 PS/km², while in rural areas it is usually less than 10 PS/km² (Ferretti et al., 2011). It indicates that the output of PSI are measurements on discrete targets distributed in the area covered by input SAR images. Obviously, if the density of the targets is low, the measurements might be hard to interpret.

Researchers have made every endeavor to retrieve as many coherent targets as possible in interferometric applications, thereby increasing the density of output products. In a PSI application, the common master scheme is used to form the corresponding interferogram stack. Inevitably, some of interferograms in the stack might be severely affected by decorrelation noise, primarily due to their long temporal and/or spatial baselines. Noting this, a series of interferometric time-series analysis methods using free interferometric combination scheme-based stacks are developed (Mora et al., 2003; Blanco-Sanchez et al., 2008; Liu et al., 2009;

* Corresponding author.

E-mail address: zk@cqu.edu.cn (K. Zhang).

Dai et al., 2013). They evaluate the decorrelation degree of every possible interferometric pair and only select the interferograms with low decorrelation for subsequent analysis, for the sake of increasing the number of coherent targets. In these methods, the criteria defined for interferogram decorrelation assessment are mainly based on temporal and/or spatial baselines. Indeed, the decorrelation phenomenon depends on many factors (e.g. image mis-coregistration) (Zhang et al., 2013); consequently, it is hard to find a uniform interferogram selection strategy for different applications. To avoid this problem, Guarnieri and Tebaldini (2008) imported a pre-processing step into interferogram stacking analysis (In this paper, this step is referred to as *phase reconstruction*). It defines a maximum likelihood estimator (MLE) based on a so-called coherence matrix which includes spatially averaged interferometric phase information of all possible input SAR image pair combinations. By resolving the MLE, the phase value on each input SAR image are reformed, thereby minimizing target decorrelation. In 2011, Ferretti et al. (2011) used statistically homogeneous pixels (SHP) to generate coherence matrices. In this way, the loss of PS during the spatial average operation can be avoided and the signal-to-noise ratio (SNR) of the phase signal contained in coherence matrices can be improved. Since then, the phase reconstruction technique has been increasingly used in interferometric applications (Lagios et al., 2013; Chaussard et al., 2014; Goel and Adam, 2014; Paradella et al., 2015).

As pointed out in Ferretti et al. (2011), phase reconstruction can be considered to be a process that figures out a set of phase values matching the weighted phase of each off-diagonal element in a coherence matrix. Indeed, the phase of a coherence matrix element is an estimate of the “true” interferometric observation between the corresponding SAR image pair. When its corresponding coherence is low, such an estimate can be significantly biased, which may exert a negative impact on the MLE process, resulting in a decrease in phase reconstruction quality. In this paper, a new approach is developed in order to address this problem. This approach converts the MLE to an optimization problem defined on a network. On the premise that the feasibility and the redundancy is guaranteed, the network is simplified by excluding the arcs corresponding to low coherence elements. In this way, the influences of severely biased interferometric phase estimates on phase reconstruction can be diminished. In addition, a targeted iterative strategy is designed based on the idea of phase linking (Guarnieri and Tebaldini, 2008) to resolve the phase reconstruction problem with respect to the simplified network. On the ground that it pursues an approximate solution rather than an optimized solution, an extremely high computational efficiency can be achieved.

2. Phase reconstruction problem and its transformation

Suppose that N input SAR images have been coregistered to a reference image, the observation vector for a given pixel p can be expressed as:

$$\mathbf{y}(p) = [y_1(p), y_2(p), \dots, y_N(p)]^T \quad (1)$$

where T stands for matrix transposition, and $y_n(p)$ represents the value of the pixel p on the n th input SAR single look complex (SLC) image. If it is assumed that neighboring pixels in the input images are statistically independent, the data coherence matrix \mathbf{C} corresponding to p can be estimated by using the following equation:

$$\mathbf{C} = \frac{1}{|\Psi|} \sum_{p \in \Psi} \bar{\mathbf{y}}(p) \bar{\mathbf{y}}(p)^H \quad (2)$$

where H represents Hermitian conjugation, and Ψ indicates the set of samples used for estimation. $\bar{\mathbf{y}}(p)$ is the normalized observation

such that $E[|\bar{\mathbf{y}}(p)|^2] = 1$ (Cao et al., 2015). Currently, there are two ways to construct \mathbf{C} . Firstly, use all the pixels within a fixed size window centered at p . Secondly, use p and its corresponding SHPs. Let \mathbf{C}_{mn} denote the m th element in \mathbf{C} . The phase value of \mathbf{C}_{mn} actually can be considered to be an estimate of p 's “true” interferometric phase with respect to the m th and the n th input SAR images, while its coherence is given by the absolute value of \mathbf{C}_{mn} .

The maximum likelihood estimator can be expressed as:

$$\hat{\Phi} = \arg \min_{\Phi} \{ \Theta^H (|\Gamma|^{-1} \circ \mathbf{C}) \Theta \} \quad (3)$$

where \circ stands for the Hadamard product, Γ is an $N \times N$ symmetric matrix with respect to the true coherence values of all interferometric pairs, $\Phi = [\theta_1, \theta_2, \dots, \theta_N]$ is the vector containing N unknown phase observations with respect to input SAR images, and $\Theta = [e^{i\theta_1}, e^{i\theta_2}, \dots, e^{i\theta_N}]$ is the complex counterpart of Φ . This is a non-linear optimization problem. The phase value of a given element in \mathbf{C} corresponds to spatially filtered interferometric observation, hence the first unknown θ_1 can be fixed to zero to decrease the complexity of the solution space. The most widely used method for phase reconstruction is the phase triangulation algorithm (PTA). It takes advantage of Broyden-Fletcher-Goldfarb-Shanno (BFGS) (Press et al., 2002) based optimization algorithms to resolve this problem, as described in Ferretti et al. (2011) and Tang et al. (2015). By using this method, an optimal solution can be retrieved. In practice, as Γ is inaccessible, its estimate (usually $|\mathbf{C}|$) is used as a substitute.

Indeed, the above problem can be transformed to an optimization problem defined on a network $G = (\mathcal{A}, \Omega)$ consisting of a set of nodes \mathcal{A} and a set of arcs Ω . \mathcal{A} consists of N elements with respect to the unknowns, while Ω has $N \times N$ elements which correspond to the elements in \mathbf{C} . The MLE problem on this network can be stated as:

$$\hat{\Phi} = \arg \min_{\Phi} \left\{ \sum_{\alpha \in \Omega} \omega(\alpha) e^{i\varphi(\alpha)} e^{-j\theta_{H(\alpha)}} e^{i\theta_{T(\alpha)}} \right\} \quad (4)$$

where

- θ_n is the unknown with respect to the node indexed by n .
- α represents an arc belonging to Ω .
- $H(\alpha)/T(\alpha)$ is the index of the head/tail node with respect to α .
- $\varphi(\alpha)$ is the phase observation defined on α , which is given by the phase of the matrix element $\mathbf{C}_{H(\alpha)T(\alpha)}$.
- $\omega(\alpha) = \{|\Gamma|^{-1}\}_{H(\alpha)T(\alpha)} \cdot |\mathbf{C}_{H(\alpha)T(\alpha)}|$. It is the weight assigned to α .

This network is referred to as a *coherence network*. Fig. 1(a) exhibits an example coherence network with five nodes. It can be clearly observed that there are $2N - 1$ arcs connecting to each node.

3. Methodology

In this section, the influence of outlying observations on a phase reconstruction process is firstly discussed. To mitigate such influence, a so-called simplified coherence network is constructed by carefully excluding potential outlying arcs from the coherence network. In order to retrieve a well-posed solution from it, the corresponding construction process ensures the network's connectivity and redundancy based on the idea of graph theory. Finally, a targeted strategy is designed to resolve the phase reconstruction problem defined on the simplified coherence network.

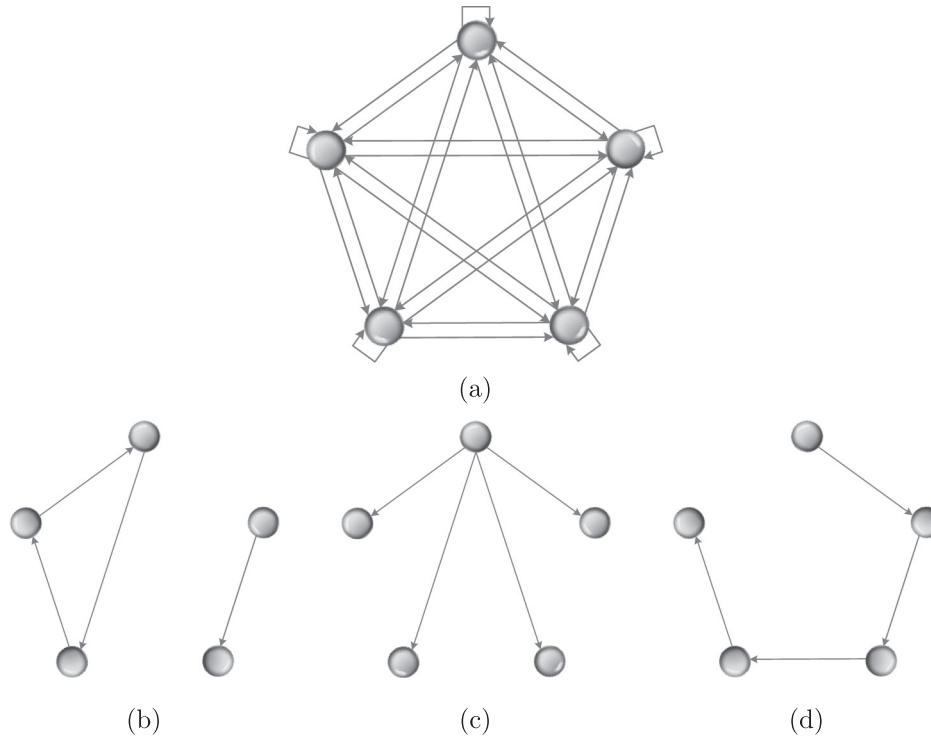


Fig. 1. An example coherence network with 5 nodes (a) and three of its sub-networks: (b) A short baseline style sub-network. (c) A PS-InSAR style sub-network. (d) A sub-network which can minimize temporal decorrelation.

3.1. Ill-posedness of a phase reconstruction problem

To some extent, the goal of a phase reconstruction process is to obtain a vector of solutions $\Phi = [\theta_1, \theta_2, \dots, \theta_N]$ from the following system:

$$\varphi(m, n) = \theta_m - \theta_n + \varepsilon_{mn} \quad m, n = 1, 2, \dots, N \quad (5)$$

where ε_{mn} is the m nth observation noise. As mentioned previously, $\varphi(m, n)$ is an estimate of the true interferometric phase between the corresponding SAR images. When its coherence value is low, such an estimate might be seriously biased and become an outlying observation. Where this is the case, the observation noise ε can be expressed as:

$$\varepsilon = u + e \quad (6)$$

where u stands for outlier noise and e indicates inlier noise. The presence of u results in the system defined in Eq. (5) being ill-posed (Mitra et al., 2013). In general, an ill-posed problem can be resolved by regularization techniques [e.g. Tikhonov regularization (Aster et al., 2013)]. Unfortunately, as the interferometric phase observation $\varphi(m, n)$ is only expressed in modulo 2π radians, traditional regularization techniques cannot be directly applied to a phase reconstruction problem.

The basic idea of regularization techniques is to retrieve a well-posed solution by means of introducing pre-defined constraints/assumptions. It must be noted that the main objective of the phase reconstruction technique is to reform the phase observations on distribute scatterers (DS). As most interferometric pairs of a DS cannot preserve interferometric coherence well, it is reasonable to assume that the majority of the observations in a phase reconstruction system contain outlier noise. If low-coherent observations can be removed as many as possible, the reliability of the solution should be improved. Consequently, the key problem is then related to: (1) the construction of a sub-network $G' = (\mathcal{A}, \mathcal{O}')$

of G by excluding arcs with low coherence, and (2) the resolution of the corresponding phase reconstruction problem:

$$\hat{\Phi} = \arg \min_{\Phi} \left\{ \sum_{\alpha \in \Omega} \omega(\alpha) e^{j\varphi(\alpha)} e^{-j\theta_{H(\alpha)}} e^{j\theta_{T(\alpha)}} \right\} \quad (7)$$

3.2. Sub-network construction

The construction of G' has to be carefully carried out. Fig. 1(b) illustrates a sub-network of Fig. 1(a). Clearly, this network is separated into two subsets due to the lack of arcs connecting them. This situation is naturally related to the phase time-series inversion problem defined on small baseline interferogram stacks, which can be resolved by applying the singular value decomposition (SVD) algorithm (Berardino et al., 2002). Unfortunately, as the optimization problem in Eq. (6) is defined on wrapped phase rather than unambiguous phase, the SVD is not valid anymore. In other words, it is not able to derive a feasible solution from this network.

Fig. 1(c) and (d) present two feasible networks with $N - 1$ arcs. In such networks, each node only connects one arc, which indicates that there are no redundant observations for the estimation. Indeed, using the solution from the network depicted by Fig. 1(c) for interferogram stacking analysis is equivalent to directly applying PSI on spatially filtered interferometric phase. In this case, the phase reconstruction process is meaningless as it does not suppress decorrelation at all. Fig. 1(d) demonstrates a sub-network from which a solution can be easily derived by a simple phase integration process. When all nodes are arranged in image acquisition order, temporal decorrelation can be minimized. However, as the physical mechanism causing decorrelation is complex (Bamler and Hartl, 1998), there is room to further improve the effect of phase reconstruction. To meet this goal, redundant arcs are required to be added into the network.

Based on the above discussion, the following strategy is developed to construct G' .

- (1) Initialize the network G' . Add N nodes into G' . Assign a connection tag $V_n = 0$ and an initial phase value $\hat{\theta}_n^{(0)} = 0$ to the n th node, where $n = 1, 2, \dots, N$.
- (2) Sort every element in $|\mathbf{C}|$ in descending order. Store the result into an array L . Let $L[i]$ denote the i th element of L and set $i = 1$. Note that $|\mathbf{C}|$ is a symmetric matrix. In this study, only the off-diagonal elements of $|\mathbf{C}|$'s lower triangular part are used for sorting, in order to improve computational efficiency.
- (3) Suppose that $|\mathbf{C}|_{mn}$ is the element corresponding to $L[i]$. Create two arcs α_1 and α_2 . Let

$$\begin{aligned} H(\alpha_1) &= m, & T(\alpha_1) &= n, & \varphi(\alpha_1) &= \angle \mathbf{C}_{mn}, \\ \omega(\alpha_1) &= \{|\mathbf{C}|^{-1}\}_{mn} \cdot |\mathbf{C}|_{mn} \end{aligned} \quad (8)$$

$$\begin{aligned} H(\alpha_2) &= n, & T(\alpha_2) &= m, & \varphi(\alpha_2) &= -\angle \mathbf{C}_{mn}, \\ \omega(\alpha_2) &= \{|\mathbf{C}|^{-1}\}_{nm} \cdot |\mathbf{C}|_{mn} \end{aligned} \quad (9)$$

- (4) Add α_1 and α_2 into \mathcal{O}' . If $i = 1$, set $V_m = 1, V_n = 1, \hat{\theta}_m^{(0)} = \angle e^{i\angle \mathbf{C}_{mn}}$, and go to (5). If $V_m = 1$ and $V_n = 0$, set $V_n = 1$ and $\hat{\theta}_n^{(0)} = \angle e^{i(\hat{\theta}_m^{(0)} - \angle \mathbf{C}_{mn})}$. If $V_n = 1$ and $V_m = 0$, set $V_m = 1$ and $\hat{\theta}_m^{(0)} = \angle e^{i(\hat{\theta}_n^{(0)} + \angle \mathbf{C}_{mn})}$. Let $i = i + 1$.

- (5) If

$$\sum_{n=1}^N V_n = N \quad (10)$$

go to (6). Otherwise, go to (3).

- (6) Let $O(n)$ denote a set including all arcs starting from n . If the following expression does not hold, go to (3).

$$|O(n)| \geq F, \quad n = 1, 2, \dots, N \quad (11)$$

where F is a predefined redundancy factor.

- (7) G' is successfully constructed. Exit. The vector $\hat{\Phi}^{(0)} = [\hat{\theta}_1^{(0)}, \hat{\theta}_2^{(0)}, \dots, \hat{\theta}_N^{(0)}]$ will be used to initialize the subsequent optimization process.

Eq. (9) guarantees that a feasible solution can be derived from the resulting network. In this paper, such a network is referred to as a *simplified coherence network* (SCN). It must be noted that the predefined redundancy factor F has to be carefully assigned. If F is too small, the redundancy of the SCN cannot be ensured. On the other hand, if F is too large, unnecessary computational resources are required for the subsequent optimization process. More significantly, outlying interferometric phase observations might be introduced, which could decrease the accuracy of the resulting estimation. Empirically, a satisfied solution can be derived from a SCN constructed using $F = 2$ or $F = 3$.

3.3. Phase reconstruction resolution

Indeed, the phase reconstruction problem defined on a SCN can be resolved by utilizing BFGS based optimization methods as well. However, such methods are not adopted in this study due to the following considerations. (1) The BFGS based methods require the first-order partial derivatives of the phase reconstruction objective function. The form of such derivatives is verbose. (2) As the dimension of the solution space of a phase reconstruction problem is large (Tens or even hundreds of input SAR images are usually used in an interferogram stacking application.), the compu-

tational costs of BFGS based methods could be extremely high, as pointed out in Ferretti et al. (2011). (3) As estimated coherence values rather than true coherence values are used in a phase reconstruction process, there is no reason to state that the optimal solution derived by BFGS based methods must provide a correct phase reconstruction. Thus, a good approximation may generally be as accurate as an exact solution. Based on the idea of phase linking, the iterative process below is designed to estimate the phase vector Φ .

$$\hat{\theta}_n^{(q)} = \sum_{\alpha \in O(n)} |\omega(\alpha)| e^{j\varphi(\alpha)} e^{j\hat{\theta}_{T(\alpha)}^{(q-1)}}, \quad n = 1, 2, \dots, N \quad (12)$$

where q is the iteration ID. There are primarily two differences between this process and the phase linking method. (1) The complex conjugate multiplication operation is only performed on the arcs of SCN rather than the full coherence matrix. A higher computational efficiency can be hence achieved in each iteration step. (2) The constraint $\theta_0 = 0$ is removed, which can accelerate the convergence of the iteration defined on a SCN.

It must be pointed out that the initial values $\hat{\theta}_1^{(0)}, \hat{\theta}_2^{(0)}, \dots, \hat{\theta}_N^{(0)}$ invoking the iteration are generated during the construction of SCN. Indeed, each $\hat{\theta}_n^{(0)}$ is obtained based on its corresponding interferometric phase with the highest coherence. Such a strategy may further speed up the iteration process. Besides, on the ground that the above process aims to retrieve an approximate solution, interferometric coherence values can be directly used as weights (Cao et al., 2015). In this case, matrix inversion operations can be avoided, thereby reducing computational workload. Moreover, a special data structure is designed and implemented for storing SCN, which is a modified version of adjacency list. Based on it, the information on each arc can be extracted efficiently. The discussion of data structure is beyond the scope of this paper. The reader is referred to Drozdek (2012) and Marli (2009) for more details.

4. Experimental results

For validation purposes the proposed SCN approach was compared with the most commonly used PTA method using both simulated data and real data. The limited-memory BFGS solver embedded in the NLOpt package was used for PTA's optimization processes. NLOpt is a free and open-source library for nonlinear optimization. It can be downloaded from <http://abinitio.mit.edu/wiki/index.php/NLOpt>. In this study, all algorithms were implemented in C++ for efficiency concerns.

4.1. Simulated data

The simulated data generation process was based on typical C-band platform configurations (e.g. wavelength: 5.6 cm, repeat cycle: 35 days). The number of input images was set to $N = 20, 21, \dots, 80$. The number of SHPs used for coherence matrix construction was set to $S = 30, 60, 90$, respectively. For a given N and S , a group of coherence matrices of 1000 points were generated. For a given point p , its "true" SAR phase observation of the n th acquisition was set to

$$\begin{cases} y_n(p) = 0 & n = 1 \\ y_n(p) = \frac{-4\pi}{\lambda R \sin \theta} \cdot B_{\perp}^n \cdot \Delta h + \frac{-4\pi}{\lambda} \cdot T^n \cdot \Delta d & n = 2, 3, \dots, N \end{cases} \quad (13)$$

where λ, θ and R are the radar wavelength, the local incidence angle, and the distance between target and sensor, respectively; B_{\perp}^n is the perpendicular baseline between the 1st and the n th SAR acquisitions, which was randomly generated by using a standard deviation $\sigma_{perp} = 200$ m; T^n is the temporal baseline, which was set to

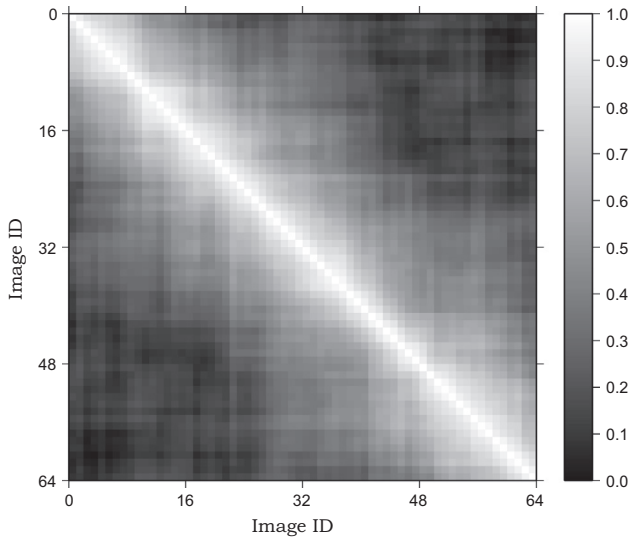


Fig. 2. A typical coherence matrix generated based on the simulated data.

$(n - 1) \times 35$ days; Δh and Δd are the randomly generated digital elevation model (DEM) error and deformation rate ($\sigma_{DEM} = 20$ m, $\sigma_{defo} = 10$ mm), respectively. For the sake of simplicity, only the temporal decorrelation noise was introduced and the interferometric coherence was directly used as phase reconstruction weights. For a given SHP, the temporal decorrelation noise on the n th acquisition was given by $\varepsilon_n = \varepsilon_{n-1} + \varepsilon_T$, where ε_T is the randomly generated noise. Its corresponding standard deviation was set to 25° . A typical coherence matrix generated via this process is shown in Fig. 2.

Fig. 3 represents the execution times of the two methods under different configurations. It can be clearly observed that the execution efficiency of each method is mainly affected by the number of input images. The PTA method exhibits a super non-linear computational complexity. On the contrary, the computational cost of the

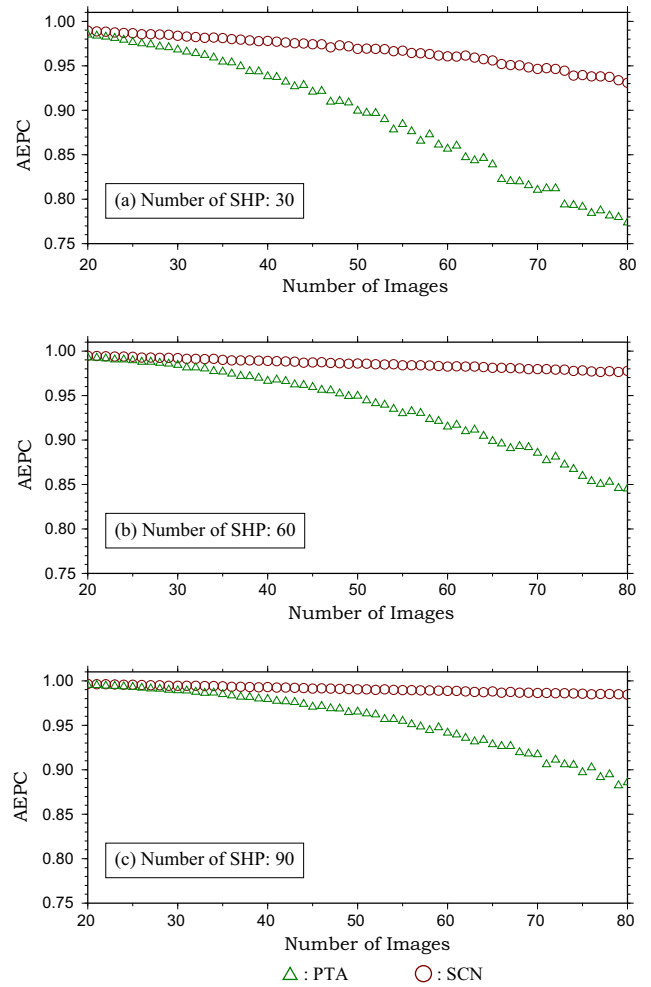


Fig. 4. The average ensemble phase coherence (AEPC) derived by the PTA and the SCN methods under different configurations.

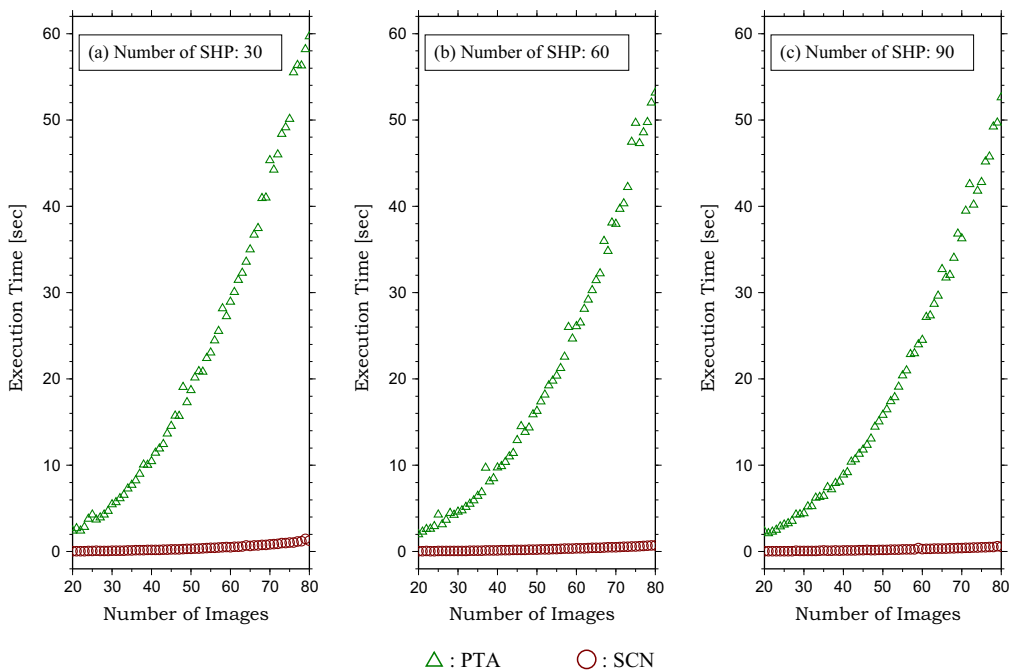


Fig. 3. The execution times required by the PTA and the SCN methods under different configurations.

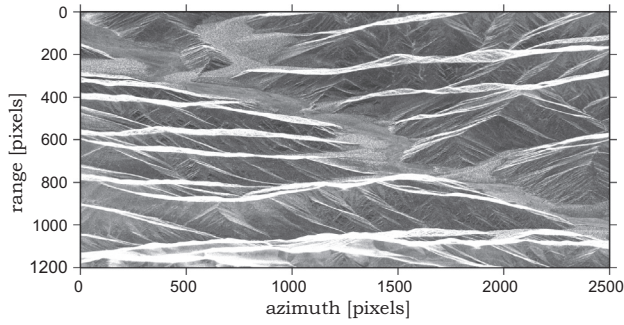


Fig. 5. The average magnitude map of the study area.

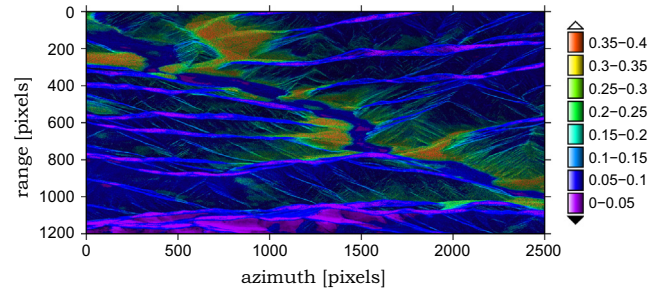


Fig. 7. The average coherence map overlaid on the average magnitude map. It was generated based on the off-diagonal elements of each DS candidate's coherence matrix.

proposed SCN method only varies slightly as the number of input images goes up. When the number of input image achieves 80, at least 52 s is required by the PTA method, while the SCN method only requires approximately 1 s. Apparently, the proposed SCN method is far superior to the PTA method in the aspect of computational performance.

In order to evaluate the reliability of the both methods, the ensemble phase coherence (EPC) corresponding to each phase reconstruction solution was calculated, which is given by:

$$\gamma(p) = \left| \frac{\sum_{n=1}^N (e^{j\hat{y}_n(p)} \cdot e^{-j\hat{y}_n(p)})}{N} \right| \quad (14)$$

where $\hat{y}_n(p)$ indicates p 's estimated phase value on the n th acquisition. EPC is ranging from 0 to 1. The higher the EPC is, the more accurate the resulting solution should be. For each group of data, an average EPC (AEPC) was calculated. The distribution of AEPC of the two methods is illustrated in Fig. 4. Clearly, the AEPC of each method decreases as the number of images increases. Moreover, a lower decreasing rate can be obtained when a larger SHP number is used for coherence matrix generation. Overall, the AEPC of the proposed SCN method is greater than that of the PTA method. When the number of input images is small, the AEPC values of the both methods are close to each other. The AEPC difference between the both methods becomes larger and larger when the number of input images arises. Consequently, it can be thought that the proposed method is capable of suppressing the influence of outlying observations effectively, especially in the case that the number of input images is large.

4.2. Real data

29 real SAR images were used to further validate the proposed SCN method. These images were acquired over the Kangxiwar

region, Xinjiang Uyghur Aptonom Rayoni, China, by the advanced synthetic aperture radar (ASAR) sensor on board the European space agency's environmental satellite (EnviSAT). Since this region is covered by rough terrains and is far away from human activities, the PS density is extremely low, which is conducive to a better representation of the effect of phase reconstruction. The image acquired on August 20, 2005 was firstly selected as the master image and cropped to a relatively small size (2500 pixels in azimuth direction 1200 pixels in range direction). The other 28 images were cautiously registered and resampled with respect to it. Subsequently, the 3-arc seconds DEM provided by the shuttle radar topography mission (SRTM) was registered to the master image. Based on the registered DEM and the precise orbit state vectors from the Doppler orbitography and radio-positioning integrated by satellite instrument (DORIS), the topographic phase contributions to the registered images were removed, respectively. The average magnitude map of the registered images is reported in Fig. 5. It can be clearly observed that the study area is dominated by rugged mountains which cause strong layover effect. Fig. 6 illustrates two differential interferograms with respect to the master image. The interferometric phase signals in the first one (Fig. 6 (a)) are completely decorrelated due to the long spans of the temporal and the perpendicular baselines. On the other hand, except for layover areas, the interferometric coherence of the second one (Fig. 6(b)) is generally preserved, as it has the shortest temporal baseline (1 repeat cycle) and a relatively small perpendicular baseline. In addition, a linear trend in range direction can be evidently seen, which primarily stems from orbital errors. For the sake of clarity, these two interferograms are referred to as "the low-coherent (LC) interferogram" and "the highly-coherent (HC) interferogram" in the subsequent discussion, respectively.

Following the idea presented in Ferretti et al. (2011), a SHP identification process was carried out for each pixel by using a

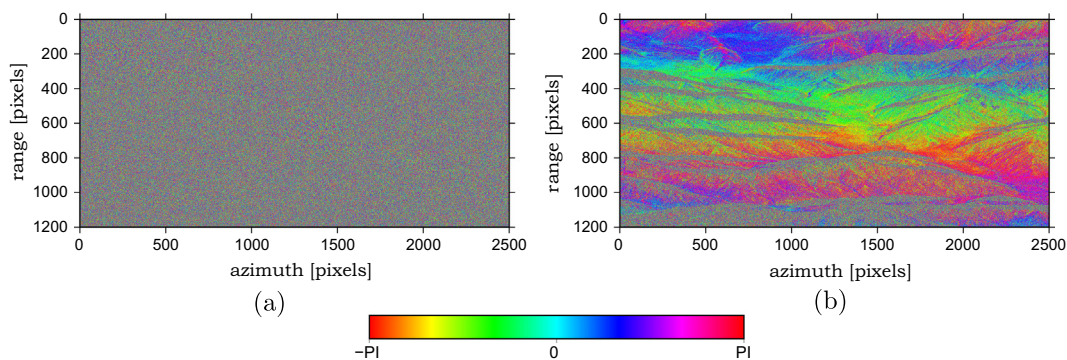


Fig. 6. Two differential interferograms with respect to the image acquired in August 20, 2005. Their temporal and perpendicular baselines are: (a) 770 days and 1130 m, (b) 35 days and 190 m. For the sake of clarity, (a) and (b) are referred to as "the low-coherent (LC) interferogram" and "the highly-coherent (HC) interferogram" in this paper, respectively.

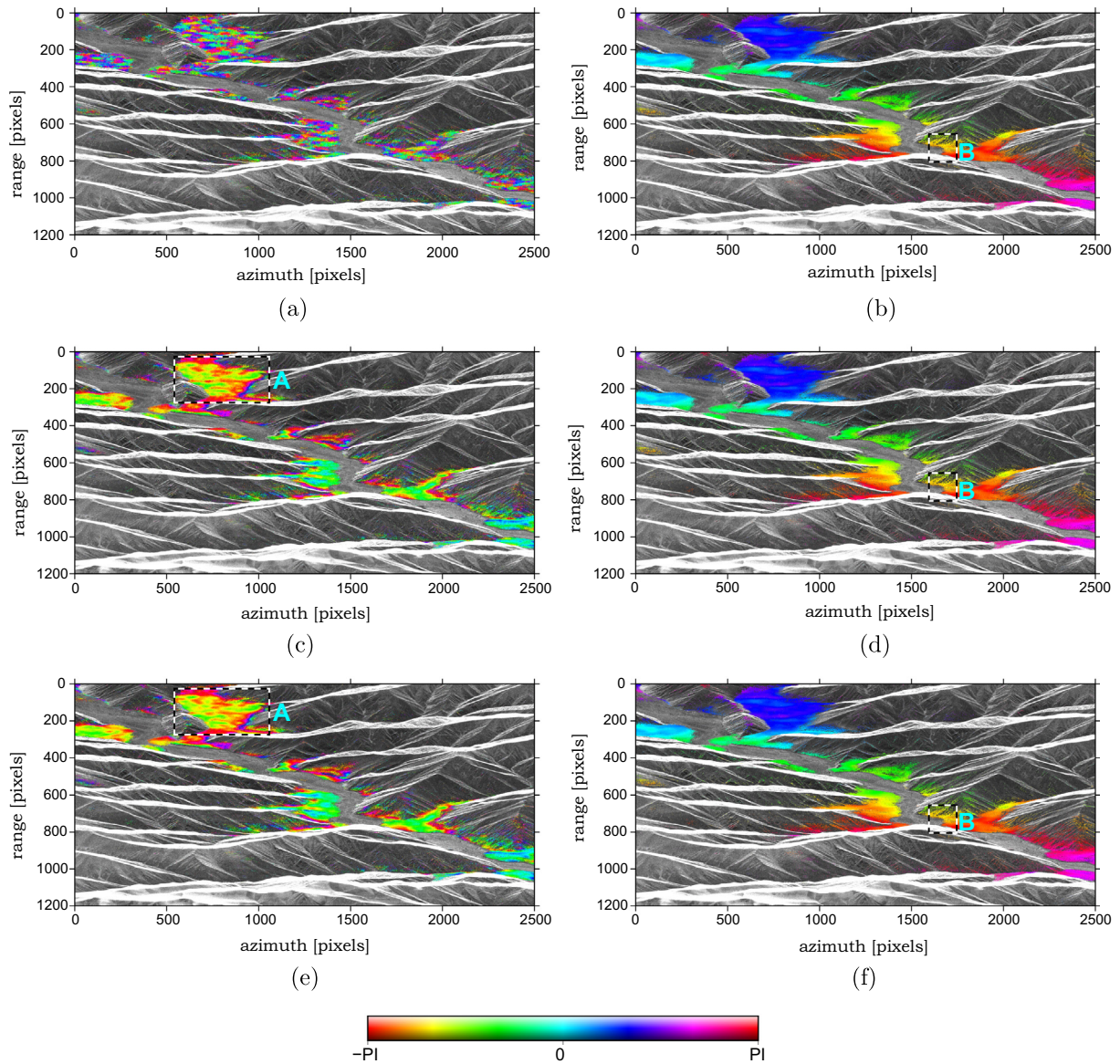


Fig. 8. (a) and (b) The filtered LC/HC interferogram overlaid on the average magnitude map. (c) and (d) The reconstructed LC/HC interferogram based on the PTA method. (e) and (f) The reconstructed LC/HC interferogram based on the proposed SCN method. In order to illustrate phase reconstruction results more intuitively, only the results on the DS candidates whose average coherence values are larger than 0.2 are shown.

window size of 51×13 . When the number of SHPs of a given pixel was greater than 20, it was recognized as a DS candidate. The coherence matrix of each DS candidate was constructed based on its SHP family, which was used for subsequently phase reconstruction operations. Overall, 2,905,944 DS candidates were obtained. Non-DS candidates were neglected, as the goal of this paper is to improve the performance of phase reconstruction. In order to exhibit the overall interferometric coherence of the input data, an average coherence map was generated based on the off-diagonal elements of each DS candidate's coherence matrix, as shown in Fig. 7. It can be observed that most regions are severely affected by the decorrelation phenomenon. Such regions are primarily distributed in upper mountains where the altitude can be up to 6200 m. The presence of unstable snow and ice should be the chief culprit causing decorrelation.

Both the proposed SCN method and the PTA method were applied to the coherence matrix of each DS candidate. In total, the SCN method and the PTA method successfully derived phase reconstruction results on 2,746,212 and 2,898,941 DS candidates,

respectively. It implies that the success rate of the SCN method is slightly lower than that of the PTA method. However, as discussed later, almost all failed SCN estimations occurs on the DS candidates located in highly decorrelated areas. In such areas, it is nearly impossible to obtain correct phase reconstruction results. Therefore, such failures would not influence the overall effect of phase reconstruction. The total computational time needed by the PTA method was around 523 min, while the SCN method only required approximately 24 min. Evidently, the proposed SCN method has a much higher computational efficiency than the PTA method.

Fig. 8(a) and (b) are the SHP-based spatial filtered versions of the LC and the HC interferograms, respectively. These two interferograms actually can be considered to be generated based on the phase reconstruction results from a fixed network similar to Fig. 1(c). It must be noted that the goal of the phase reconstruction technique is to reshape the phase observations in areas with moderate coherence. Therefore, in order to illustrate the effect of phase reconstruction more intuitively, only the results on the DS candidates whose average coherence values are larger than 0.2 are

shown. As expected, the interferometric signals contained in the filtered HC interferogram are highly correlated. On the contrary, it is hard to extract any valid interferometric information from the filtered LC interferogram. By using the phase reconstruction solutions from the PTA method, a new LC/HC interferogram was generated, as presented in Fig. 8(c)/(d). No manifest difference between the PTA HC interferogram and the filtered HC interferogram can be observed, which demonstrates that the phase reconstruction technique preserves the interferometric characteristics of highly correlated pairs. Unlike the filtered LC interferogram, the PTA's counterpart consists of “low-pass” pattern interferometric signals, implying that decorrelation noise is effectively suppressed by the phase reconstruction technique. The SCN LC and the SCN HC interferograms are indicated in Fig. 8(e) and (f), respec-

tively. Overall, they are comparable to the PTA's counterparts. Hence, the effectiveness of the proposed SCN method is validated.

For a better comparison between the SCN and the PTA methods, their corresponding LC and HC interferometric results over two representative areas (marked as A and B in Fig. 8) were extracted, respectively. Fig. 9 shows the PTA LC and the SCN LC interferometric signals in area A. It can be clearly observed that the SCN result (Fig. 9(b)) contains less high-frequency signals compared to the PTA result (Fig. 9(a)). To some extent, a phase reconstruction operation can be considered to be a spatial filter in temporal domain. As the goal of such a filter is to suppress high-frequency signals, the SCN solution is expected to be closer to the correct one. The filtered, the PTA and the SCN HC interferometric signals in area B are illustrated in Fig. 10. The SCN HC result (Fig. 10(c)) is remarkably sim-

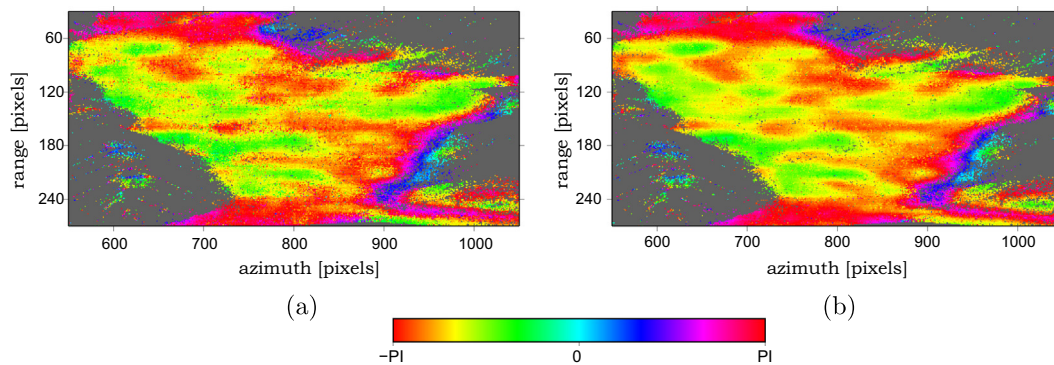


Fig. 9. The reconstructed LC interferometric signals from the PTA method (a) and the SCN method (b) over the area marked by A in Fig. 5.

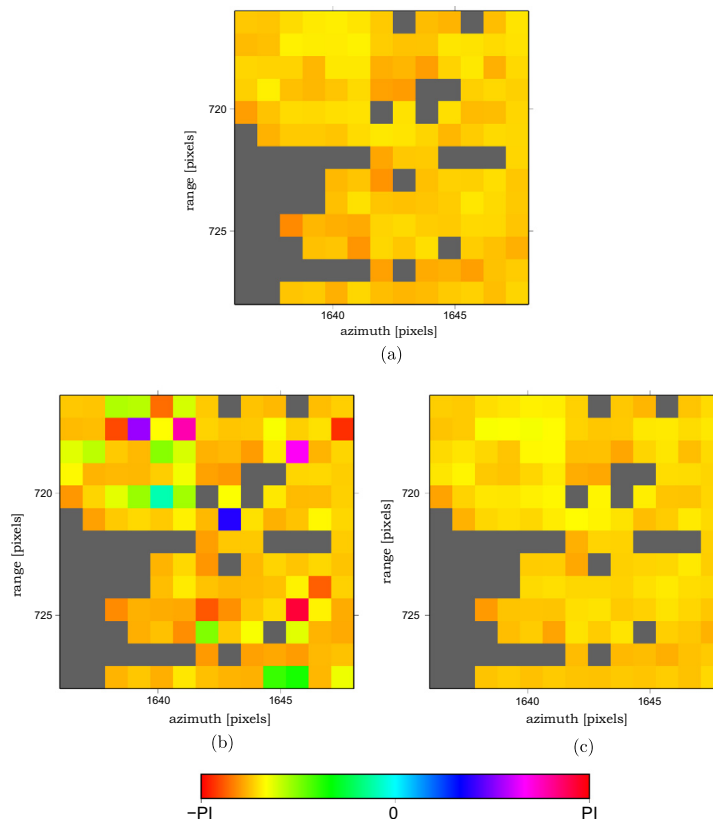


Fig. 10. (a) The interferometric signals extracted from the filtered HC interferogram over the area marked by B in Fig. 5. (b) From the reconstructed HC interferogram of PTA. (c) From the reconstructed HC interferogram of SCN.

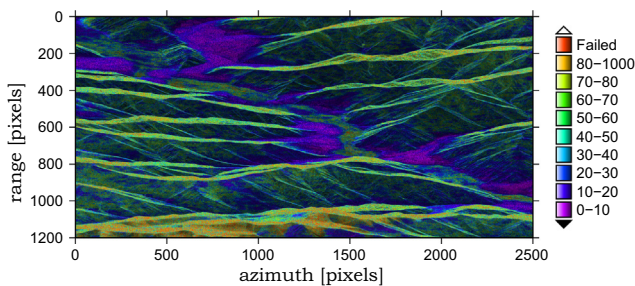


Fig. 11. A map of the SCN iteration number with respect to each DS candidate.

ilar to the filtered HC result (Fig. 10(a)). On the other hand, some abrupt signals are clearly observed in the PTA result presented in Fig. 10(b). Since the HC interferogram preserves a good coherence, a reconstructed HC interferogram is expected to be close to the filtered HC interferogram. In this sense, the SCN solution is superior to the PTA solution.

To better examine the performance of the proposed SCN method, a maximum iteration number of 1000 was used and the iteration number required for resolving the SCN defined on each DS candidate was recorded. An iteration number map can be hence generated, as shown in Fig. 11. It can be observed that the proposed method converges successfully on most of DS candidates and the failed SCN estimations are only located in highly decorrelated areas. Moreover, this map is highly correlated to the average coherence map shown in Fig. 7. In the areas where interferometric coherence is generally preserved, the proposed SCN method can converge within 30 iterations. Therefore, when a relatively smaller maximum iteration number is used, the proposed method is still able to effectively complete the phase reconstruction. Where this is the case, the execution time required by the proposed SCN method can be further reduced.

5. Concluding remarks

In this paper, a new phase reconstruction approach based on simplified coherence network is proposed. With the use of the SCN, the adverse impacts of seriously biased coherence matrix elements on phase reconstruction can be reduced. A targeted iterative strategy for solving the SCN phase reconstruction problem is designed and implemented as well. Since it aims to derive an approximate solution rather than the optimal one, its computational efficiency is remarkably high. By applying the proposed method to real SAR data, its excellent performance is confirmed.

Acknowledgments

The authors are very grateful to ESA for providing EnviSAT/ASAR data. This work is jointly supported by the National Natural Science Foundation of China (Grant Nos. 41404027, 41461164004), the International Science & Technology Cooperation Program of China (Grant No. 2105DFR21100), and the Fundamental Research Funds for the Central Universities (Grant No. 106112013cdjzr160005).

References

Aster, R.C., Thurber, C.H., Borchers, B., 2013. *Parameter Estimation and Inverse Problems*, second ed. Elsevier, MA, USA.

- Bamler, R., Hartl, P., 1998. Synthetic aperture radar interferometry. *Inverse Prob.* 14 (4), R1–R54.
- Berardino, P., Fornaro, G., Lanari, R., Sansosti, E., 2002. A new algorithm for surface deformation monitoring based on small baseline differential SAR interferograms. *IEEE Trans. Geosci. Rem. Sens.* 40 (11), 2375–2383.
- Blanco-Sanchez, P., Mallorqui, J., Duque, S., Monells, D., 2008. The coherent pixels technique (CPT): an advanced DInSAR technique for nonlinear deformation monitoring. *Pure Appl. Geophys.* 165 (6), 1167–1193.
- Cao, N., Lee, H., Jung, H.C., 2015. Mathematical framework for phase-triangulation algorithms in distributed-scatterer interferometry. *IEEE Geosci. Rem. Sens. Lett.* 12 (9), 1838–1842.
- Chaussard, E., Wdowinski, S., Cabral-Cano, E., Amelung, F., 2014. Land subsidence in central Mexico detected by ALOS InSAR time-series. *Rem. Sens. Environ.* 140, 94–106.
- Ciampalini, A., Bardi, F., Bianchini, S., Frodella, W., Ventisette, C.D., Moretti, S., Casagli, N., 2014. Analysis of building deformation in landslide area using multisensor PSInSARTM technique. *Int. J. Appl. Earth Observat. Geoinform.* 33, 166–180.
- Crossetto, M., Monserrat, O., Cuevas-Gonzalez, M., Devanthy, N., Crippa, B., 2016. Persistent scatterer interferometry: a review. *ISPRS J. Photogramm. Rem. Sens.* 115, 78–89.
- Dai, K., Liu, G., Yu, B., Jia, H., Ma, D., Wang, X., 2013. Detecting subsidence along a high speed railway by ultrashort baseline TCP-InSAR with high resolution images. *ISPRS – Int. Arch. Photogramm. xl-7/w2 (7)*, 61–65.
- Drozdek, A., 2012. *Data Structures and Algorithm in C++*, fourth ed. Cengage Learning India, Pacific Grove, USA.
- Ferretti, A., Fumagalli, A., Novali, F., Prati, C., Rocca, F., Rucci, A., 2011. A new algorithm for processing interferometric data-stacks: SqueeSAR. *IEEE Trans. Geosci. Rem. Sens.* 49 (9), 3460–3470.
- Ferretti, A., Prati, C., Rocca, F., 2000. Nonlinear subsidence rate estimation using permanent scatterers in differential SAR interferometry. *IEEE Trans. Geosci. Rem. Sens.* 38 (5), 2202–2212.
- Ferretti, A., Prati, C., Rocca, F., 2001. Permanent scatterers in SAR interferometry. *IEEE Trans. Geosci. Rem. Sens.* 39 (1), 8–20.
- Goel, K., Adam, N., 2014. A distributed scatterer interferometry approach for precision monitoring of known surface deformation phenomena. *IEEE Trans. Geosci. Rem. Sens.* 52 (9), 5454–5468.
- Graniczny, M., Colombo, D., Kowalski, Z., Przylucka, M., Zdanowski, A., 2015. New results on ground deformation in the Upper Silesian Coal Basin (southern Poland) obtained during the DORIS Project (EU-FP 7). *Pure Appl. Geophys.* 172 (11), 3029–3042.
- Guarnieri, A., Tebaldini, S., 2008. On the exploitation of target statistics for SAR interferometry applications. *IEEE Trans. Geosci. Rem. Sens.* 46 (11), 3436–3443.
- Hooper, A., Zebker, H., Segall, P., Kampes, B., 2004. A new method for measuring deformation on volcanoes and other natural terrains using InSAR persistent scatterers. *Geophys. Res. Lett.* 31 (23), 275–295.
- Lagios, E., Sakkas, V., Novali, F., Bellotti, F., Ferretti, A., Vlachou, K., Dietrich, V., 2013. SqueeSARTM and GPS ground deformation monitoring of Santorini Volcano (1992–2012): tectonic implications. *Tectonophysics* 594, 38–59.
- Liu, G., Buckley, S., Ding, X., Chen, Q., Luo, X., 2009. Estimating spatiotemporal ground deformation with improved permanent-scatterer radar interferometry. *IEEE Trans. Geosci. Rem. Sens.* 47 (8), 2762–2772.
- Marli, D.S., 2009. *Data Structures Using C++*, second ed. Course Technology, Boston, USA.
- Mitra, K., Veeraraghavan, A., Chellappa, R., 2013. Analysis of sparse regularization based robust regression approaches. *IEEE Trans. Signal Process.* 61 (5), 1249–1257.
- Mora, O., Mallorqui, J., Broquetas, A., 2003. Linear and nonlinear terrain deformation maps from a reduced set of interferometric SAR images. *IEEE Trans. Geosci. Rem. Sens.* 41 (10), 2243–2253.
- Paradella, W.R., Ferretti, A., Mura, J.C., Colombo, D., Gama, F.F., Tamburini, A., Santos, A.R., Novali, F., Galo, M., Camargo, P.O., 2015. Mapping surface deformation in open pit iron mines of Carajás Province (Amazon Region) using an integrated SAR analysis. *Eng. Geol.* 193, 61–78.
- Peltier, A., Bianchi, M., Kaminski, E., Komorowski, J.-C., Rucci, A., Staudacher, T., 2010. PSInSAR as a new tool to monitor pre-eruptive volcano ground deformation: validation using GPS measurements on Piton de la Fournaise. *Geophys. Res. Lett.* 37 (12), L12301.1–L12301.5.
- Press, W., Teukolsky, S., Vetterling, W., Flannery, B., 2002. *Numerical Recipes in C++*. Cambridge University Press, United Kingdom.
- Tang, P., Chen, F., Guo, H., Tian, B., Wang, X., Ishwaran, N., 2015. Large-area landslides monitoring using advanced multi-temporal InSAR technique over the Giant Panda Habitat, Sichuan, China. *Rem. Sens.* 7 (7), 8925–8949.
- Terranova, C., Ventura, G., Vilaro, G., 2015. Multiple causes of ground deformation in the Napoli metropolitan area (Italy) from integrated persistent scatterers DInSAR, geological, hydrological, and urban infrastructure data. *Earth-Sci. Rev.* 146, 105–119.
- Zhang, K., Ge, L., Li, X., Ng, A.H.-M., 2013. Monitoring ground surface deformation over the North China Plain using coherent ALOS PALSAR differential interferograms. *J. Geodesy* 87 (3), 253–265.